

Abstract

We perform a geomagnetic event simulation using a newly developed magnetohydrodynamic with adaptively embedded particle-in-cell (MHD-AEPIC) model. We have developed effective criteria to identify reconnection sites in the magnetotail and cover them with the PIC model. The MHD-AEPIC simulation results are compared with Hall MHD and ideal MHD simulations to study the impacts of kinetic reconnection at multiple physical scales. At the global scale, the three models produce very similar SYM-H and SuperMag Electrojet (SME) indexes, which indicates that the global magnetic field configurations from the three models are very close to each other. At the mesoscale we compare the simulations with in situ Geotail observations in the tail. All three models produce reasonable agreement with the Geotail observations. The MHD-AEPIC and Hall MHD models produce tailward and earthward propagating fluxropes, while the ideal MHD simulation does not generate flux ropes in the near-earth current sheet. At the kinetic scales, the MHD-AEPIC simulation can produce a crescent shape distribution of the electron velocity space at the electron diffusion region which agrees very well with MMS observations near a tail reconnection site. These electron scale kinetic features are not available in either the Hall MHD or ideal MHD models. Overall, the MHD-AEPIC model compares well with observations at all scales, it works robustly, and the computational cost is acceptable due to the adaptive adjustment of the PIC domain.

1 Introduction

A geomagnetic storm is a major disturbance of Earth's magnetosphere that occurs when a significant amount of energy is deposited into the geospace. The most widely used and successful simulation tools to study the geomagnetic storms are based on the magnetohydrodynamic (MHD) description, which is computationally feasible to solve. The first global MHD models were developed in the 1980s (LeBoeuf et al., 1981; Wu et al., 1981; Brecht et al., 1981, 1982). Later on, models with more advanced numerical algorithms have been developed, such as the Lyon-Fedder-Mobarry (LFM) (J. G. Lyon et al., 1986; J. Lyon et al., 2004), the OpenGGCM (Raeder et al., 1995, 1996) and the GUMICS (Grand Unified Magnetosphere Ionosphere Coupling Simulation) model (Janhunen, 1996).

In this paper, we use the University of Michigan's Space Weather Modeling Framework (SWMF (Tóth et al., 2012)) which also includes an MHD model, the Block Adaptive-Tree Solar-wind Roe-type Upwind Scheme (BATS-R-US) (Powell et al., 1999) as its global magnetosphere (GM) component. The SWMF has been applied to many storm event simulations (Tóth et al., 2007; Glocer et al., 2009; Haiducek et al., 2017), which is also been selected as the physics-based model at the Space Weather Prediction Center based on a thorough model comparison (Pulkkinen et al., 2013).

Magnetic reconnection plays a key role in the magnetosphere both at the dayside and in the tail. Despite all the successful applications MHD models have achieved, magnetic reconnection in the global MHD models relies on either Hall resistivity, or ad hoc anomalous resistivity, or simply numerical resistivity. None of these approximations truly describe the physical processes responsible for collisionless reconnection. It is very important to properly represent kinetic reconnection physics in a global simulation and check if it plays an important role in contributing to the larger scale processes that eventually produce geomagnetic disturbances and space weather effects. Furthermore, the MHD approximation assumes that the distribution functions of the ions and electrons are Maxwellian. Numerous observations suggest that this condition is violated especially near the magnetic reconnection sites (L.-J. Chen et al., 2016; Burch et al., 2016; Hwang et al., 2019; Lotekar et al., 2020).

The MHD with embedded Particle-In-Cell (MHD-EPIC) model (Daldorff et al., 2014) enables kinetic physics to be introduced into a global MHD model. The MHD-EPIC

66 model has been successfully used to study the interaction between the Jovian wind and
 67 Ganymede’s magnetosphere (Tóth et al., 2016; Zhou et al., 2019, 2020); flux transfer events
 68 (FTEs) at the Earth’s dayside magnetopause (Y. Chen et al., 2017); Mars’ magnetotail
 69 dynamics (Y. Ma et al., 2018) and the dawn-dusk asymmetries discovered at the Mer-
 70 cury’s magnetotail (Y. Chen et al., 2019). However, the iPIC3D (Markidis et al., 2010)
 71 code, which is the PIC model used in the MHD-EPIC simulations, can only run on a fixed
 72 Cartesian grid. The magnetotail (and the associated current sheet that contains the re-
 73 connection sites) typically exhibits a flapping motion (Tsutomu & Teruki, 1976; Volw-
 74 erk et al., 2013) during a geomagnetic storms. Covering the whole domain of interest
 75 where reconnection can occur in the magnetotail would require a very large PIC grid and
 76 would result in a massive computational cost. This may be feasible for a short simula-
 77 tion time (up to an hour or so) but geomagnetic storms that usually happen last for days,
 78 the computational cost would become prohibitive.

79 To tackle this problem, we have developed the MHD with Adaptively Embedded
 80 PIC (MHD-AEPIC) algorithm. Shou et al. (2021) introduces this idea and verifies that
 81 by dynamically changing the region of the computational domain where the PIC model
 82 is applied, the numerical solution doesn’t change essentially compared to a larger fixed
 83 PIC domain. In this paper, we further improve this method and make it more flexible:
 84 1. The size and shape of the active PIC regions can be adapted during the runtime; 2.
 85 The adaptation of the active PIC region is fully automatic. To realize the first feature,
 86 instead of iPIC3D, we use the FLEKS (Flexible Exascale Kinetic Simulator) (Y. Chen
 87 et al., 2021) as the PIC model. FLEKS inherits all numerical algorithms from MHD-EPIC,
 88 and also accommodates an adaptive PIC grid that allows PIC cells to be turned on and
 89 off during the simulation. In addition, FLEKS employs a particle splitting and merg-
 90 ing scheme to improve the simulation efficiency and accuracy. FLEKS is described in
 91 more detail in Section 2.2.

92 We have developed a reliable and efficient algorithm to identify potential recon-
 93 nection sites in the magnetotail using three local criteria. The criteria are easy to com-
 94 pute and provide the information to the FLEKS code to adapt its grid to cover the re-
 95 connection sites. This newly developed MHD-AEPIC model is applied to simulate a mag-
 96 netic storm. The SWMF simulation involves BATSRUS, FLEKS, the ionosphere elec-
 97 trodynamics model RIM (Ridley et al., 2004) and the inner magnetosphere model RCM
 98 (Wolf et al., 1982; Toffoletto et al., 2003). This is the first simulation of a real event with
 99 kinetic reconnection physics in the magnetotail scaling from the global scales of the mag-
 100 netosphere to the electron scales near the reconnection sites.

101 The computational methods are described in Section 2, the demonstration of the
 102 adaptation feature and comparisons between models and observations are shown in Sec-
 103 tion 3 and we summarize in Section 4.

104 2 Methods

105 2.1 Global Magnetosphere Model: BATS-R-US

106 The Block-Adaptive Tree Solar-wind Roe-type Upwind Scheme (BATS-R-US) is
 107 used as the Global Magnetosphere (GM) model in our simulation. In the Hall MHD and
 108 MHD-AEPIC simulations in this paper, the Hall MHD equations (Tóth et al., 2008) are
 109 solved. The Hall term is handled with a semi-implicit scheme. The spatial discretiza-
 110 tion uses a 2nd order accurate TVD scheme with the Artificial Wind Riemann solver (Sokolov
 111 et al., 1999) and the Koren limiter (Koren, 1993) with $\beta = 1.2$. The hyperbolic clean-
 112 ing (Dedner et al., 2003) and eight-wave scheme (Powell et al., 1999) are used to keep
 113 the magnetic field approximately divergence-free.

114 The Hall MHD equations with a separate electron pressure equation are

$$\frac{\partial \rho}{\partial t} = -\nabla \cdot (\rho \mathbf{u}) \quad (1)$$

$$\frac{\partial(\rho \mathbf{u})}{\partial t} = -\nabla \cdot \left[\rho \mathbf{u} \mathbf{u} + (p + p_e) \bar{I} + \frac{B^2}{2\mu_0} \bar{I} - \frac{\mathbf{B}\mathbf{B}}{\mu_0} \right] \quad (2)$$

$$\frac{\partial e}{\partial t} = -\nabla \cdot \left[(\epsilon + p) \mathbf{u} + p_e \mathbf{u}_e + \mathbf{u}_e \cdot \left(\frac{\mathbf{B}^2}{\mu_0} \bar{I} - \frac{\mathbf{B}\mathbf{B}}{\mu_0} \right) \right] + p_e \nabla \cdot \mathbf{u}_e \quad (3)$$

$$\frac{\partial \mathbf{B}}{\partial t} = -\nabla \times \left[\mathbf{u}_e \times \mathbf{B} + \frac{\nabla p_e}{ne} \right] \quad (4)$$

$$\frac{\partial p_e}{\partial t} = -\nabla \cdot (p_e \mathbf{u}_e) - (\gamma - 1) p_e \nabla \cdot \mathbf{u}_e \quad (5)$$

115 where \bar{I} is the identity matrix, ρ is the mass density, \mathbf{u} is the plasma bulk velocity, \mathbf{B}
 116 is the magnetic field, p_e is the electron pressure, p is the ion pressure and $\mathbf{j} = \nabla \times \mathbf{B} / \mu_0$
 117 is the current density. The Hall velocity and electron bulk velocity are defined as

$$\mathbf{v}_H = -\frac{\mathbf{j}}{ne} = -\frac{M_i}{e} \frac{\mathbf{j}}{\rho} \quad (6)$$

$$\mathbf{u}_e = \mathbf{u} + \mathbf{v}_H \quad (7)$$

118 where $n = \rho / M_i$ is the number density, M_i is the ion mass, and e is the elementary charge.
 119 The total energy density is defined as

$$e = \epsilon + \frac{B^2}{2\mu_0} = \frac{1}{2} \rho \mathbf{u}^2 + \frac{p}{\gamma - 1} + \frac{B^2}{2\mu_0} \quad (8)$$

120 where $\epsilon = \rho \mathbf{u}^2 / 2 + p / (\gamma - 1)$ is the hydrodynamic energy density of the ions and $\gamma =$
 121 $5/3$ is the adiabatic index. The thermal energy density of the electrons is $\epsilon_e = p_e / (\gamma -$
 122 $1)$. We note that the $e + \epsilon_e$ is conserved both analytically and numerically as the non-
 123 conservative source terms $\pm p_e \nabla \cdot \mathbf{u}$ in equations (3) and (5) cancel out. Apart from $(\rho, \mathbf{u}, \mathbf{B}, p, p_e)$,
 124 other variables are derived quantities.

125 The continuity equation (1), momentum equation (2), energy equation (3) and elec-
 126 tron pressure equation (5) are solved with an explicit time stepping scheme. In the in-
 127 duction equation (4), the convection term $\mathbf{u} \times \mathbf{B}$ and pressure gradient term $\nabla p_e / ne$
 128 are solved using an explicit scheme, while the Hall term $\mathbf{v}_H \times \mathbf{B}$ is advanced with an
 129 implicit scheme. The Hall MHD equations introduce whistler mode wave, which has a
 130 characteristic wave speed inversely proportional to the wavelength. The shortest wave-
 131 length that exists in a numerical simulation is proportional to the cell size Δx , so the
 132 fastest whistler wave speed in a simulation is proportional to $1/\Delta x$. The time step in
 133 a fully explicit scheme is limited by the Courant-Friedrichs-Lewy (CFL) condition: $\Delta t <$
 134 $\Delta x / c_{\max}$, where c_{\max} is the fastest wave speed, which leads to a time step proportional
 135 to $1/(\Delta x)^2$. We use a semi-implicit scheme (Tóth et al., 2012) to handle the stiff Hall
 136 term in the induction equation, so that the time step of the explicit part is only limited
 137 by the fast magnetosonic wave speed instead of the whistler speed.

138 A three-dimensional block-adaptive Cartesian grid is used to cover the entire com-
 139 putational domain $-224R_E < x < 32R_E$, $-128R_E < y, z < 128R_E$ in GSM coord-
 140 inates. The Hall effect is restricted to $x \in [-100R_E, 20R_E]$, $|y| < 30R_E$ and $|z| <$
 141 $20R_E$ box region excluding a sphere of radius $3R_E$ centered at the Earth to speed up
 142 the simulation. Outside this region the Hall effect is neglected by setting $\mathbf{v}_H = 0$. The
 143 cell size in the magnetotail is refined to the resolution with $\Delta x = 1/4R_E$. About four-
 144 teen millions cells are used in total.

145 At the inner boundary $r = 2.5R_E$, the density is calculated by the formula $\rho_{\text{inner}} =$
 146 $28 + 0.1\text{CPCP amu/cm}^3$, where CPCP is the average of the northern and southern cross
 147 polar cap potentials measured in keV. This boundary condition has been used success-
 148 fully in previous geomagnetic storm simulations (Pulkkinen et al., 2013). The pressure

149 and magnetic field \mathbf{B}_1 have zero gradient at the inner boundary, while the radial veloc-
 150 ity is set to zero and the tangential velocity is calculated from the corotation and the
 151 $\mathbf{E} \times \mathbf{B}$ drift, where the electric field \mathbf{E} is provided by the Ridley Ionosphere Model (RIM)
 152 (Ridley et al., 2004).

153 2.2 Particle-in-cell Model: FLEKS

154 The FLEKS (Flexible Exascale Kinetic Simulator) (Y. Chen et al., 2021) is used
 155 as the particle-in-cell (PIC) model (PC component in the SWMF) to resolve kinetic physics.
 156 FLEKS uses the same two-way coupling method as MHD-EPIC (Daldorff et al., 2014)
 157 and the Gauss’s law satisfying energy-conserving semi-implicit method (GL-ECSIM) (Y. Chen
 158 & Tóth, 2019) for the PIC solver. To enable the adaptation in MHD-AEPIC, FLEKS
 159 introduces an adaptive grid that allows changing simulation region dynamically. Figure
 160 1 shows a schematic plot of the adaptive grid.

161 FLEKS provides a particle merging and splitting scheme to maintain the number
 162 of particles per cell within bounds. Merging particles in a cell with high number of par-
 163 ticles can improve load-balancing and speed up simulation, while splitting particles in
 164 a cell with few particles can reduce noise and improve accuracy for the PIC simulation.
 165 This feature is very useful keeping the number of particles per cell about uniform dur-
 166 ing a long geomagnetic storm simulation.

167 2.3 Selection Criteria of PIC Regions

168 As described in the previous section, FLEKS allows patches to be turned on and
 169 off during the simulation. To make the active PIC patches only cover the regions of in-
 170 terest, where magnetic reconnection is happening or will be triggered soon, the MHD
 171 model should locate these regions and pass this information to FLEKS. Finding the lo-
 172 cations of magnetic reconnection sites can be done in various ways including tracing field
 173 lines (Glocer et al., 2016). For sake of efficiency and generality, here we use local crite-
 174 ria based on the local MHD solution only.

175 Magnetic reconnection usually happens in current sheets where the current den-
 176 sity j is strong and the magnetic field B is weak. In particular, the field B_\perp that is per-
 177 pendicular to the current \mathbf{j} should be close to zero, while the guide field parallel to the
 178 current can be non-zero. We define the following non-dimensional relation as our first
 179 criterion

$$\frac{J\Delta x}{B_\perp + \varepsilon} = \frac{J^2\Delta x}{|\mathbf{J} \times \mathbf{B}| + J\varepsilon} > c_1 \quad (9)$$

180 where $\mathbf{J} = \mu_0\mathbf{j} = \nabla \times \mathbf{B}$ and ε is a small dimensional constant in units of the mag-
 181 netic field introduced to avoid dividing by zero. We use $\varepsilon = 1$ nT in our simulations pre-
 182 sented here, which is much smaller than the typical magnetic field intensity in the tail
 183 current sheet. Δx is the local cell size that is used in calculating the curl of the magnetic
 184 field, so that $J\Delta x$ is the jump of the transverse magnetic field between neighboring grid
 185 cells. We set $c_1 = 0.8$ in this work to select the cells that are close to the reconnection
 186 sites.

187 While criterion (9) works quite well in general, we sometimes find that it selects
 188 the axis of flux ropes, or O-lines, in addition to X-lines, especially if ε is very small. Re-
 189 connection does not occur at O-lines, so we developed a second criterion that distinguishes
 190 X- and O-lines based on the divergence of the magnetic field curvature vector:

$$[\nabla \cdot (\mathbf{b} \cdot \nabla \mathbf{b})](\Delta x)^2 > c_2 \quad (10)$$

191 where $\mathbf{b} = \mathbf{B}/|\mathbf{B}|$ is a unit vector along the magnetic field. We use $c_2 = -0.1$ to iden-
 192 tify X-lines where the curvature vectors point away from the X-line, so their divergence
 193 is positive.

194 The above two criteria are identifying potential magnetic reconnection sites through
 195 local plasma properties in a general scenario. However, current sheets in the solar wind
 196 can also satisfy those two criteria. To make the selection more selective, we need to in-
 197 troduce a third criterion to exclude the volume outside the magnetosphere. Observations
 198 show that specific entropy is two orders of magnitude larger in the magnetosphere than
 199 in the magnetosheath (X. Ma & Otto, 2014) and our simulations properly reproduce these
 200 properties. Here we use the specific entropy as the third criterion:

$$\frac{p}{\rho^\gamma} > c_3 \quad (11)$$

201 where p is the plasma thermal pressure, ρ is the plasma density, and $\gamma = 5/3$ is the ra-
 202 tio of the specific heats (Birn et al., 2006, 2009). Different from the c_1 and c_2 introduced
 203 above, this criterion is dimensional and we use the threshold value $c_3 = 0.02 \text{ nPa/cm}^{-3\gamma}$.

204 The three criteria combined can identify X-lines in the magnetotail well. To make
 205 the active PIC region large enough around the X-lines, we flag all patches where all three
 206 criteria are met, and then activate all patches within a distance L_x , L_y and L_z from these
 207 flagged patches in the x , y and z directions, respectively. We use $L_x = 4R_E$ and $L_y =$
 208 $L_z = 2R_E$ in this work.

209 Each MPI process of BATS-R-US calculates the above criteria on their respective
 210 sub-domains overlapping with the PIC grid and activate the patches of the PIC grid where
 211 all 3 criteria are satisfied. Then the processors collect the information: a PIC patch is
 212 activated if any of the BATS-R-US processes activated it. Since the status of all PIC patches
 213 (on/off) is stored in each MPI processor of BATS-R-US, using the default logical array
 214 would consume a lot of memory. To reduce the memory use, the status is stored by a
 215 single bit, which is 32 times smaller than the size of the default logical variable in For-
 216 tran. The information is conveniently collected with the bitwise "or" operator `MPI BOR`
 217 used in the `MPI_ALLREDUCE` call.

218 2.4 Ionospheric Electrodynamics Model: RIM

219 The Ionospheric Electrodynamics (IE) is simulated by the Ridley Ionosphere Model
 220 (RIM) (Ridley et al., 2004) that solves a Poisson-type equation for the electric poten-
 221 tial on a 2-D spherical grid. In this work, the grid resolution is set to 2° in both longi-
 222 tude and latitude directions. The lower latitude boundary is at 10° where the electric
 223 potential is set to zero.

224 The BATS-R-US and RIM models are two-way coupled every 5 seconds. To cal-
 225 culate the Poisson-type equation, RIM obtains the field-aligned currents (FAC) calcu-
 226 lated at $3R_E$ from the BATS-R-US model and maps them down to its grid. The F10.7
 227 flux is also an input parameter of RIM that is used together with the FAC to calculate
 228 the particle precipitation and conductances based on an empirical model. The electric
 229 field calculated by the RIM is mapped back to the inner boundary of BATS-R-US to ob-
 230 tain the $\mathbf{E} \times \mathbf{B}/B^2$ velocity for its inner boundary condition. The cross polar cap po-
 231 tentials (CPCP, (the difference of the maximum and minimum potentials in the two hemi-
 232 spheres) are also sent to BATS-R-US to set the density at the inner boundary.

233 2.5 Inner Magnetosphere Model: RCM

234 The Inner Magnetosphere (IM) is modeled by the Rice Convection Model (RCM)
 235 (Wolf et al., 1982; Toffoletto et al., 2003). The standard RCM settings are used, includ-
 236 ing an exponential decay term with a 10-hour e-folding rate. The decay term makes the
 237 Dst index recover better after strong storms.

238 The RCM model is one-way coupled with RIM and two-way coupled with BATS-
 239 R-US every 10 seconds. RIM sends the electric potential to RCM, where it is used to

240 advect the field lines with the $\mathbf{E} \times \mathbf{B} / B^2$ drift. In the two-way coupling between BATS-
 241 R-US and RCM, BATS-R-US identifies the closed field line regions and calculates field
 242 volume integrals of pressure and density (De Zeeuw et al., 2004). The integrated pres-
 243 sure and density are applied to RCM as the outer boundary condition with the assump-
 244 tion of 90% H^+ and 10% O^+ number density composition. From RCM to BATS-R-US,
 245 the GM grid cell centers are traced to the RCM boundary along the magnetic field lines
 246 (De Zeeuw et al., 2004) and the BATS-R-US pressure and density are pushed towards
 247 the RCM values with a 20s relaxation time.

248 3 3D Global Simulation with Kinetic Physics in the Magnetotail

249 3.1 Simulation Setup

250 We apply the MHD-AEPIC method to the geomagnetic storm event of Aug. 6. 2011
 251 with an observed minimum $\text{Dst} = -126$ nT. Previous modeling works show frequent flap-
 252 ping motion of the magnetotail current sheet during the storm (Tsutomu & Teruki, 1976;
 253 Volwerk et al., 2013), so the adaptive embedding feature is perfect for only covering the
 254 current sheet during the simulation. We start our simulation at 2011-08-05 15:00:00 and
 255 end it at 2011-08-06 07:00:00. This time range covers the main phase and the early re-
 256 covering phase of the storm when the largest geomagnetic impact happens. The solar
 257 wind inputs are shown in Figure 2. First the BATS-R-US and RIM models are run to
 258 reach a quasi-steady state after 50k iteration steps using local time stepping. Figure
 259 3 shows the plasma density along with the different refinement level boundaries of the
 260 AMR grid in the meridional plane for the steady state solution. Then the SWMF is switched
 261 to a time-accurate mode with FLEKS and RCM models turned on. The computational
 262 domain of FLEKS is determined by the selection criteria introduced above. For sake of
 263 comparison, we also conduct two other simulations without FLEKS: one with Hall MHD
 264 model and the other with ideal MHD model.

265 3.2 PIC Region Adaptation

266 In this subsection, we highlight the utility and efficiency of the adaptive embed-
 267 ding scheme. Figure 4 illustrates how the PIC region is changing over the simulation.
 268 Panels (a)-(f) are snapshots from six different times. The color contours show the j_y com-
 269 ponent of the current density on the meridional plane to show the magnetospheric cur-
 270 rent system. Boundaries of the active PIC region are shown by the gray isosurface. Snap-
 271 shots 4 (a) and (b) are taken before the sudden commencement of the storm. At this time,
 272 the IMF B_z is pointing northward and the solar wind speed is about 400 km/s. From
 273 the isosurface plot, the PIC region is covering the tail current sheet tilting southward.
 274 In Figure 4 (b), the tail current sheet is kinked and the PIC region adjusts its shape to
 275 accommodate the tail current sheet. Snapshots 4 (c)-(f) are taken after the sudden com-
 276 mencement of the storm. Here we observe a much compressed magnetosphere as well as
 277 an enhanced current density. In the last two snapshots, the tail current sheet is tilting
 278 northward and it is well covered by the PIC region. From the snapshots, we can con-
 279 clude that the PIC region selection criteria work well in identifying the tail current sheet,
 280 which can make the PIC region accommodate with the flapping motion of the magne-
 281 totail. The red line in Figure 4 (g) is the volume of the active PIC region (smoothed ev-
 282 ery 60 seconds), the Dst index is also presented in the background for reference. The vol-
 283 ume of the PIC region increase after the sudden commencement and start dropping at
 284 the recovering phase. This reflects the tail current system intensity related to the solar
 285 wind condition. Notice that the volume is less than $2000 R_E^3$ for the entire storm sim-
 286 ulation, which is only about 1.4% of a large PIC box extending from $-100R_E$ to $-10R_E$
 287 on x direction and $-20R_E$ to $20R_E$ in y and z directions. This implies that the MHD-
 288 AEPIC method saves substantial amount of computational resources.

289

3.3 Global Scale: Geomagnetic Indexes

290

291

292

293

294

295

296

297

298

299

To evaluate the models' performance at the global scale, we use the SYM-H and SME as evaluation metrics. The SYM-H index approximates the symmetric portion of the northward component of the magnetic field near the equator based on measurements at six ground magnetometer stations. This index characterizes the strength of the ring current (Ganushkina et al., 2017) and it is an indicator of storm activity. The SuperMAG electrojet (SME) index is an indicator of substorms and auroral power (Newell & Gjerloev, 2011). SME utilizes more than 100 ground magnetometer stations at geomagnetic latitudes between $+40^\circ$ and $+80^\circ$, which resolves the large and extreme events more effectively than the traditional Auroral Electrojets (AE) index (Davis & Sugiura, 1966; Bergin et al., 2020).

300

301

302

303

304

305

306

307

308

309

310

311

312

313

314

In our model, the simulated SYM-H is calculated by evaluating the Biot-Savart integral at the center of the Earth from all currents in the simulation domain. Calculating SME is more complicated: the magnetic field disturbances are calculated at the positions of the 100+ ground magnetometer stations and the simulated SME is obtained following the SuperMAG procedure. From Figure 5, the MHD-AEPIC produces geomagnetic indexes close to the other two MHD models. The SYM-H plot shows that the initial, main and recovery phases of the storm event are reproduced by all three models reasonably well. However, the models cannot reproduce the lowest SYM-H values that correspond to the strongest observed geomagnetic perturbations. This feature can also be observed in the SME plots: all three models produce increased auroral electrojets, however the second and third enhancements are weaker than the observed values. The geomagnetic indexes demonstrate that introducing kinetic physics in the magnetotail does not change the global configuration of the simulated magnetosphere significantly relative to the ideal and Hall MHD simulations. It is to be seen if this trend persists for other storms, especially extreme events.

315

3.4 Mesoscale: Magnetotail Dynamics

316

317

318

319

320

321

322

323

324

325

326

327

328

329

330

331

332

333

334

335

336

337

338

339

340

During the storm event, the Geotail spacecraft was in the magnetotail at $x \approx -29 R_E$ crossing the equatorial plane and approaching to the meridional plane. Figure 6 shows the magnetic field and ion moments observed by Geotail and compares them with the ideal-MHD, Hall-MHD and MHD-AEPIC simulations. The MHD-AEPIC model shows a reasonable agreement with the Geotail number density observation before $t = 2011-08-06 00:00$, including the current sheet crossing event between $t = 2011-08-05 22:00$ and $t = 2011-08-05 23:00$ while the Hall-MHD model overestimates the ion number density substantially. However, all three models generate much higher number density than observed after $t = 2011-08-06 00:00$. None of the three models show perfect agreement with the magnetic field observations. The B_x component gives us information about which side of the current sheet the satellite is. The comparison plot shows that the virtual satellites in the simulations are all on the opposite side of the current sheet than Geotail before $t = 2011-08-05 22:00$. Between $t = 2011-08-05 23:00$ and $t = 2011-08-06 01:00$, Geotail is crossing the current sheet from the north side to the south side, and this is captured by all three models. However, the next current sheet crossing at around $t = 2011-08-06 01:30$ is not captured by MHD-AEPIC and ideal-MHD. The Hall-MHD simulations produces a similar structure but with a 30-minute time shift. The B_y and B_z components give information about flux rope structures. All three models provide good agreement with the observation in terms of overall field magnitude, while it is difficult to tell which one is better in capturing fine details. Geotail observed a B_z reversal along with a relatively strong core B_y at around $t = 2011-08-06 05:00$, which indicates a flux rope. A similar structure is produced by MHD-AEPIC with a 30-minute delay, while there is no similar signal from the ideal-MHD and Hall-MHD simulations. Geotail observed high ion speed around 1000 km/s at $t = 2011-08-06 02:00$ and $t = 2011-08-06 03:00$. The MHD-AEPIC model only generates around 500 km/s ion speeds. Although the ideal-

341 MHD and Hall-MHD models can produce maximum ion speeds around 1000 km/s, they
 342 also generate large scale oscillations that are not present in the observations. Overall,
 343 introducing kinetic physics in the magnetotail did not improve plasma and magnetic fea-
 344 tures compared to the ideal MHD simulation at the mesoscale. The Hall MHD simula-
 345 tion, on the other hand, produces significantly more oscillations than observed in mul-
 346 tiple time periods.

347 Since Geotail only observes along a single trajectory, it cannot provide insight into
 348 the full dynamics of the magnetotail. To compare the different models, we plot results
 349 on 2-D surfaces. Figure 7 shows the magnetosphere simulation results from three mod-
 350 els at the same time 2011-08-05 19:40:00. Figure 7 (a1), (b1) and (c1) show the x
 351 component of the ion bulk velocity and magnetic field lines in the meridional plane ($-80 R_E <$
 352 $x < -5 R_E$ and $-20 R_E < z < 10 R_E$) from MHD-AEPIC, Hall MHD and ideal MHD
 353 simulations, respectively. The global configurations of the magnetosphere share a lot of
 354 similarities but there are several differences as well. All three models give a southward
 355 tilted magnetotail that is compressed most in the z direction at around $x = -40 R_E$
 356 as a result of the IMF structure. In terms of the reconnection feature, all three models
 357 generate X-lines in the tail current sheet at around $x = -20 R_E$ and $z = -5 R_E$. Di-
 358 verging reconnection ion jets are generated at the major X-line for all three models.

359 To analyze physical quantities in the current sheet better, we extract the quanti-
 360 ties along a surface where $B_x = 0$ and project this surface to the $x - y$ plane for plot-
 361 ting. The bottom row in Figure 7 shows the z coordinate of the center of the current sheet.
 362 The structure is similar as in the meridional plane plots: the current sheets are at $z \approx$
 363 0 near Earth and at $z \approx -15 R_E$ at far tail for MHD-AEPIC and Hall MHD models,
 364 while $z \approx -12 R_E$ for ideal MHD. Figure 7 (a2)-(c2) show the ion bulk flow speed on
 365 the current sheet surface. There are significant differences among the three models in
 366 the earthward ion flow structures. For ideal MHD, the earthward ion flow is distributed
 367 roughly symmetrically at $-3 R_E < y < 3 R_E$. The earthward ion jet generated by Hall
 368 MHD can only be observed on the dawn side at $-5 R_E < y < 0$. The MHD-AEPIC
 369 simulation produces earthward ion jet both on the dawn and dusk sides. However, the
 370 ion jet on the dawn side is further away from the earth than the jets on the dusk side.
 371 Also, the earthward ion jets can be observed from $-5 R_E$ to $7 R_E$ in the y direction, which
 372 agrees with the observations that earthward flows are observed at a wide range of y val-
 373 ues (Angelopoulos et al., 1994).

374 Although the earthward ion flow from MHD-AEPIC is different from pure MHD
 375 models, the similar magnetic field structure and current sheet position indicate that these
 376 snapshots from different models represent the same physical state of the magnetosphere.
 377 Hence, it is valid to examine the flux rope features based on these results. As first pro-
 378 posed to be formed in the Earth's magnetotail (Schindler, 1974), magnetic flux ropes are
 379 reported to be closely related to magnetic reconnection by various observations and sim-
 380 ulations (Hones Jr et al., 1984; Slavin et al., 1989; Daughton et al., 2006; Markidis et
 381 al., 2013). The observational characteristics of the flux ropes are a pair of positive and
 382 negative B_z signatures with a core magnetic field B_y in between. Hence, we plot the B_z
 383 and $|B_y|$ components on the current sheet surface in Figure 7(a-c)(2-3). Panels (c3) and
 384 (c4) shows only one flux rope at $-40 R_E$ and there is no evidence indicating flux rope
 385 exists at the near earth plasma sheet from $-40 R_E$ to the Earth based on the ideal MHD
 386 model results. The Hall MHD and MHD-AEPIC give very different flux rope occurrence
 387 (Figure 7 (a-b)(3-4)) from ideal MHD. In addition to the moving directions of the flux
 388 ropes, the diameter of the flux ropes also varies: the earthward flux ropes are observed
 389 as smaller ones. This difference has been reported in a thorough analysis of Geotail ob-
 390 servations (Slavin et al., 2003). By examining the flux ropes as a mesoscale feature, we
 391 can conclude that by modeling the reconnection physics better, the MHD-AEPIC and
 392 Hall MHD simulations produce more flux ropes in the magnetotail than ideal MHD as
 393 well as distinguish two types of the flux ropes. However, there is no evidence support-

ing that MHD-AEPIC can produce better mesoscale features than Hall MHD. This could be the case because the spatial scale of the flux ropes is much larger than the kinetic scale which PIC model is resolving.

3.5 Kinetic Scale: Electron Velocity Distribution Function

In this subsection, we will demonstrate that the kinetic physics at the reconnection site is also properly captured by the MHD-AEPIC model. The magnetic reconnection is regarded as one of the most fundamental physical processes to transfer energy from magnetic field to plasma. Since the launch of the Magnetospheric Multiscale (MMS) mission (Burch et al., 2016), magnetic reconnection has been observed at the electron scale during multiple satellite crossings of the electron diffusion region (EDR) (Webster et al., 2018). The EDR encounters exhibit electron agyrotropy, which can be recognized by a crescent-shaped electron distributions (Torbert et al., 2018).

Figure 8 compares the MHD-AEPIC simulation with MMS observations (Hwang et al., 2019). Panel (a) is a contour plot of ion bulk velocity in the meridional plane at $t = 2011-08-05\ 23:20:00$. The ion jets, a clear signature of magnetic reconnection, are shown by the blue and red colors. Panels (b) and (d) show the electron velocity distribution functions (VDF) from the model and the MMS observation. The simulation VDF of the electrons is collected inside an ellipsoid region centered at $(-30.6, 0.5, -0.9) R_E$ with principle semi-axes $(0.3, 2.5, 0.3) R_E$ in the (x, y, z) directions, respectively. The choice of the ellipsoid shape is based on panel (c) that shows where the MMS observations were taken with respect to the reconnection site according to Figure 2 by Hwang et al. (2019). The red circle in panel (a) is the cross section of the ellipsoid on the meridional plane. To compare with observation by MMS3 (Hwang et al., 2019) at $(-18.1, 7.30, 0.66) R_E$ is presented aside. Although the simulation and observation are not from the same event and the EDR is not at the same position, the electron data is collected at a similar location relative to the X-point and the $y-z$ coordinates from the simulation are closely aligned with the $M-N$ coordinates from the observation (see panels (a) and (c)).

This suggests that we can directly compare the two VDF plots in panels (b) and (d), and they indeed agree very well. The agreement is not only qualitative, but in fact quantitative. Since we are using an ion-electron mass ratio of 100 in the PIC code, the simulation electron velocity is multiplied by $\sqrt{\frac{m_{i,\text{real}}}{m_{e,\text{real}}} / \frac{m_{i,\text{simulation}}}{m_{e,\text{simulation}}}} \approx \sqrt{18.36} \approx 4.28$ to be comparable with the observations. In both panels the velocity distribution extends to $\pm 40,000$ km/s in the z direction and $(-40,000, 20,000)$ km/s in the y direction. A non-Maxwellian core distribution can also be clearly identified in both panels at $-20,000$ km/s $< v_y < 10,000$ km/s) and $|v_z| < 10,000$ km/s. Hence, we can conclude that an MHD-AEPIC global simulation can generate electron phase space distribution that is very close to the MMS observation, and resolves the electron scales in reconnection physics.

4 Conclusions and Discussions

In this paper, we introduced a newly developed magnetohydrodynamic with adaptively embedded particle-in-cell (MHD-AEPIC) model. The MHD-AEPIC allows PIC grid cells to be turned on and off during the simulation based on the physical criteria provided. Different from the previous MHD-EPIC model, which requires a fixed Cartesian box to cover the PIC region, the MHD-AEPIC model enables PIC regions moving with the reconnection sites to save computational resources substantially. During the main phase of the storm, from $t = 2011-08-06\ 00:05:00$ to $t = 2011-08-06\ 02:54:00$, when the volume of the PIC domain is about $1500 R_E^3$. The relative timings are the following: 72.72% of CPU time is used on FLEKS, 13.26% is for BATS-R-US and 10.35% is taken by the coupling between FLEKS and BATS-R-US. The rest 3.67% of CPU time is consumed by RIM, RCM and the overhead of the SWMF. For the entire 16-hour geomagnetic storm simulation, the total wall time is 256.29 hours on 5600 CPU cores.

444 We also introduced three physics based criteria to identify the reconnection regions
445 in the magnetotail. To demonstrate the feasibility of the MHD-AEPIC model, we have
446 performed a geomagnetic storm event simulation with kinetic physics embedded for the
447 first time. The flapping motion of the magnetotail current sheet during the geomagnetic
448 storm highlights the advantage of the adaptation feature of the MHD-AEPIC model.

449 We have also simulated the same event using Hall MHD and ideal MHD models
450 and compared the three models at multiple physical scales. We examined the global scale
451 features by comparing the SYM-H and SME indexes which reflect the equatorial and auroral
452 region disturbances, respectively. All three models properly capture the global scale
453 disturbances such as the main phase of the storm or the increase of the auroral electro-
454 jet. However, all three models fail to produce the strongest intensity for the geoin-
455 dices. Hence no significant difference is found among the three different models at the global
456 scale for this event. This indicates that the global magnetosphere configuration from the
457 three models are very close, the kinetic model embedded in the magnetotail does not im-
458 prove the global scale feature for this geomagnetic storm. If this trend persists for other
459 storms, especially extreme events, is still to be investigated.

460 We analyze the mesoscale features by comparing the magnetic field components
461 and ion profiles between the Geotail observation and the simulations. All three models
462 show fairly good agreement with the Geotail observations, however, none of the three
463 models can match all features such as all the current sheet crossing or flux rope signa-
464 tures. The Hall MHD simulation shows more oscillations than observed during a few time
465 periods. In this storm event, MHD-AEPIC and ideal MHD models produce similar agree-
466 ment with the in-situ observations of Geotail.

467 In addition to comparing with the Geotail observations, we also compare the three
468 models with respect to flux rope structures in the current sheet. Only one major flux rope
469 can be observed from the ideal MHD simulation at the selected time, while Hall MHD
470 and MHD-AEPIC can produce flux ropes at a wider range in the dawn-dusk direction.
471 The difference of two types of the flux ropes: earth-ward with smaller spatial scale and
472 tail-ward with a larger spatial scale is also illustrated by the MHD-AEPIC simulations,
473 in agreement with several observations (Slavin et al., 2003).

474 The electron scale kinetic physics is well reproduced by the MHD-AEPIC model.
475 We collect electron macro-particle velocities at the same side of the electron diffusion
476 region as the MMS3 satellite did (Hwang et al., 2019). The velocity distribution func-
477 tions show excellent agreement between the simulation and the MMS3 observation. This
478 demonstrates that MHD-AEPIC can properly produce the electron scale features within
479 a single self-consistent global model while simulating a complete geomagnetic storm event.
480 In this particular simulation, including the kinetic reconnection physics does not improve
481 agreement with observations at meso- and global scales. This suggests that in this storm
482 event, the magnetosphere is mostly driven by the external solar wind and interplanetary
483 magnetic field and not by the internal reconnection dynamics.

484 It is to be investigated if the kinetic physics can have a more pronounced influence
485 on the physical condition of the magnetosphere when the external drivers are relatively
486 constant. Another important question is to compare the impact of kinetic versus numer-
487 ical reconnection during extreme events. In addition to studying the Earth's magneto-
488 sphere, we also expect the novel MHD-AEPIC model will find its applications in vari-
489 ous collisionless plasma systems that form small regions where kinetic effects are impor-
490 tant inside a large spatial domain.

491 Data Availability Statement

492 The Geotail data is publicly available at Data ARchives and Transmission System
493 (DARTS) of Institute of Space and Astronautical Science (ISAS) (<https://darts.isas.jaxa.jp>).

494 The MMS observation plot is acquired with consent from Dr. K.-J. Hwang (jhwang@swri.edu).
 495 The SWMF code (including BATS-R-US and FLEKS) is publicly available through the
 496 csem.engin.umich.edu/tools/swmf web site after registration. The simulation output and
 497 scripts used for generating figures in this paper can be obtained online through the Uni-
 498 versity of Michigan’s Deep Blue Data repository, which is specifically designed for U-
 499 M researchers to share their research data and to ensure its long-term viability.

500 Acknowledgments

501 We thank Dr. Qusai Al Shidi at the University of Michigan for the script calculating the
 502 SME index using interpolated virtual magnetometer data from BATS-R-US. This work
 503 was primarily supported by NSF PRE-EVENTS grant No. 1663800. We also acknowl-
 504 edge support from the NASA DRIVE Center at the University of Michigan under grant
 505 NASA 80NSSC20K0600. We acknowledge the use of computational resources provided
 506 by an NSF LRAC allocation at the Texas Advanced Computing Center (TACC) at The
 507 University of Texas at Austin.

508 References

- 509 Angelopoulos, V., Kennel, C. F., Coroniti, F. V., Pellat, R., Kivelson, M. G.,
 510 Walker, R. J., ... Gosling, J. T. (1994). Statistical characteristics of bursty
 511 bulk flow events. *J. Geophys. Res.*, *99*, 21,257.
- 512 Bergin, A., Chapman, S. C., & Gjerloev, J. W. (2020). Ae, dst, and their supermag
 513 counterparts: The effect of improved spatial resolution in geomagnetic indices.
 514 *Journal of Geophysical Research: Space Physics*, *125*(5), e2020JA027828.
- 515 Birn, J., Hesse, M., & Schindler, K. (2006). Entropy conservation in simulations of
 516 magnetic reconnection. *Physics of plasmas*, *13*(9), 092117.
- 517 Birn, J., Hesse, M., Schindler, K., & Zaharia, S. (2009). Role of entropy in magneto-
 518 tail dynamics. *Journal of Geophysical Research: Space Physics*, *114*(A9).
- 519 Brecht, S., Lyon, J., Fedder, J., & Hain, K. (1981). A simulation study of east-west
 520 IMF effects on the magnetosphere. *Geophys. Res. Lett.*, *8*, 397–400.
- 521 Brecht, S., Lyon, J., Fedder, J., & Hain, K. (1982). A time-dependent three-
 522 dimensional simulation of the earth’s magnetosphere: Reconnection events.
 523 *J. Geophys. Res.*, *87*, 6098–6108.
- 524 Burch, J. L., Torbert, R. B., Phan, T. D., Chen, L.-J., Moore, T. E., Ergun, R. E.,
 525 ... Chandler, M. (2016). Electron-scale measurements of magnetic reconnection
 526 in space. *Science*, *352*, 6290. doi: 10.1126/science.aaf2939
- 527 Chen, L.-J., Hesse, M., Wang, S., Gershman, D., Ergun, R., Pollock, C., ... others
 528 (2016). Electron energization and mixing observed by mms in the vicinity of
 529 an electron diffusion region during magnetopause reconnection. *Geophysical*
 530 *Research Letters*, *43*(12), 6036–6043.
- 531 Chen, Y., & Tóth, G. (2019). Gauss’s law satisfying energy-conserving semi-implicit
 532 particle-in-cell method. *J. Comput. Phys.*, *386*, 632. doi: 10.1016/j.jcp.2019.02
 533 .032
- 534 Chen, Y., Tóth, G., Cassak, P., Jia, X., Gombosi, T. I., Slavin, J., ... Peng, B.
 535 (2017). Global three-dimensional simulation of earth’s dayside recon-
 536 nection using a two-way coupled magnetohydrodynamics with embedded
 537 particle-in-cell model: initial results. *J. Geophys. Res.*, *122*, 10318. doi:
 538 10.1002/2017JA024186
- 539 Chen, Y., Toth, G., Zhou, H., & Wang, X. (2021). Fleks: A flexible particle-in-
 540 cell code for multi-scale plasma simulations. *Earth and Space Science Open*
 541 *Archive*. doi: doi.org/10.1002/essoar.10508070.1
- 542 Chen, Y., Tóth, G., Jia, X., Slavin, J. A., Sun, W., Markidis, S., ... Raines, J. M.
 543 (2019). Studying dawn-dusk asymmetries of mercury’s magnetotail using mhd-
 544 epic simulations. *Journal of Geophysical Research: Space Physics*, *124*(11),

- 8954-8973.
- 545 Daldorff, L. K. S., Tóth, G., Gombosi, T. I., Lapenta, G., Amaya, J., Markidis, S., &
546 Brackbill, J. U. (2014). Two-way coupling of a global Hall magnetohydrody-
547 namics model with a local implicit Particle-in-Cell model. *J. Comput. Phys.*,
548 *268*, 236. doi: 10.1016/j.jcp.2014.03.009
- 549 Daughton, W., Scudder, J., & Karimabadi, H. (2006). Fully kinetic simulations
550 of undriven magnetic reconnection with open boundary conditions. *Physics of*
551 *Plasmas*, *13*(7), 072101.
- 552 Davis, T. N., & Sugiura, M. (1966). Auroral electrojet activity index *ae* and its uni-
553 versal time variations. *Journal of Geophysical Research*, *71*(3), 785–801.
- 554 De Zeeuw, D., Sazykin, S., Wolf, R., Gombosi, T., Ridley, A., & Tóth, G. (2004).
555 Coupling of a global MHD code and an inner magnetosphere model: Initial
556 results. *J. Geophys. Res.*, *109*(A12), 219. doi: 10.1029/2003JA010366
- 557 Dedner, A., Kemm, F., Kröner, D., Munz, C., Schnitzer, T., & Wesenberg, M.
558 (2003). Hyperbolic divergence cleaning for the MHD equations. *J. Comput.*
559 *Phys.*, *175*, 645–673.
- 560 Ganushkina, N., Jaynes, A., & Liemohn, M. (2017). Space weather effects produced
561 by the ring current particles. *Space Science Reviews*, *212*(3), 1315–1344.
- 562 Glocer, A., Dorelli, J., Tóth, G., Komar, C. M., & Cassak, P. A. (2016). Sepa-
563 rator reconnection at the magnetopause for predominantly northward and
564 southward IMF: techniques and results. *J. Geophys. Res.*, *120*, 5377. doi:
565 10.1002/2015JA021417
- 566 Glocer, A., Tóth, G., Ma, Y. J., Gombosi, T., Zhang, J.-C., & Kistler, L. M. (2009).
567 Multifluid Block-Adaptive-Tree Solar wind Roe-type Upwind Scheme: Mag-
568 netospheric composition and dynamics during geomagnetic storms – initial
569 results. *J. Geophys. Res.*, *114*, A12203. doi: 10.1029/2009JA014418
- 570 Haiducek, J. D., Welling, D. T., Ganushkina, N. Y., Morley, S. K., & Ozturk, D. S.
571 (2017). Swmf global magnetosphere simulations of january 2005: Geomagnetic
572 indices and cross-polar cap potential. *Space Weather*, *15*(12), 1567–1587.
- 573 Hones Jr, E., Birn, J., Baker, D., Bame, S., Feldman, W., McComas, D., ... Tsuru-
574 tani, B. (1984). Detailed examination of a plasmoid in the distant magnetotail
575 with isee 3. *Geophysical research letters*, *11*(10), 1046–1049.
- 576 Hwang, K.-J., Choi, E., Dokgo, K., Burch, J., Sibeck, D., Giles, B., ... others (2019).
577 Electron vorticity indicative of the electron diffusion region of magnetic recon-
578 nection. *Geophysical research letters*, *46*(12), 6287–6296.
- 579 Janhunen, P. (1996). GUMICS-3: A global ionosphere-magnetosphere coupling
580 simulation with high ionospheric resolution. In *Proceedings of the ESA 1996*
581 *symposium on environment modelling for space-based applications* (pp. 233–
582 239). ESA SP-392.
- 583 Koren, B. (1993). A robust upwind discretisation method for advection, diffusion
584 and source terms. In C. Vreugdenhil & B.Koren (Eds.), *Numerical methods for*
585 *advection-diffusion problems* (p. 117). Vieweg, Braunschweig.
- 586 LeBoeuf, J. N., Tajima, T., Kennel, C. F., & Dawson, J. M. (1981). Global sim-
587 ulations of the three-dimensional magnetosphere. *Geophys. Res. Lett.*, *8*, 257–
588 260.
- 589 Lotekar, A., Vasko, I., Mozer, F., Hutchinson, I., Artemyev, A., Bale, S., ... others
590 (2020). Multisatellite mms analysis of electron holes in the earth’s magneto-
591 tail: Origin, properties, velocity gap, and transverse instability. *Journal of*
592 *Geophysical Research: Space Physics*, *125*(9), e2020JA028066.
- 593 Lyon, J., Fedder, J., & Mobarry, C. (2004). The Lyon-Fedder-Mobarry (LFM) global
594 MHD magnetospheric simulation code. *J. Atmos. Sol-Terr. Phys.*, *66*, 1333.
- 595 Lyon, J. G., Fedder, J., & Huba, J. (1986). The effect of different resistivity models
596 on magnetotail dynamics. *J. Geophys. Res.*, *91*, 8057–8064.
- 597 Ma, X., & Otto, A. (2014). Nonadiabatic heating in magnetic reconnection. *Journal*
598 *of Geophysical Research: Space Physics*, *119*(7), 5575–5588.
- 599

- 600 Ma, Y., Russell, C. T., Toth, G., Chen, Y., Nagy, A. F., Harada, Y., ... others
 601 (2018). Reconnection in the martian magnetotail: Hall-mhd with embedded
 602 particle-in-cell simulations. *Journal of Geophysical Research: Space Physics*,
 603 *123*(5), 3742–3763.
- 604 Markidis, S., Henri, P., Lapenta, G., Divin, A., Goldman, M., Newman, D., &
 605 Laure, E. (2013). Kinetic simulations of plasmoid chain dynamics. *Physics of
 606 Plasmas*, *20*(8), 082105.
- 607 Markidis, S., Lapenta, G., & Rizwan-Uddin. (2010). Multi-scale simulations of
 608 plasma with ipic3d. *Mathematics and Computers in Simulation*, *80*, 1509–
 609 1519. doi: 10.1016/j.matcom.2009.08.038
- 610 Newell, P., & Gjerloev, J. (2011). Evaluation of supermag auroral electrojet indices
 611 as indicators of substorms and auroral power. *Journal of Geophysical Research:
 612 Space Physics*, *116*(A12).
- 613 Powell, K., Roe, P., Linde, T., Gombosi, T., & De Zeeuw, D. L. (1999). A solution-
 614 adaptive upwind scheme for ideal magnetohydrodynamics. *J. Comput. Phys.*,
 615 *154*, 284-309. doi: 10.1006/jcph.1999.6299
- 616 Pulkkinen, A., Rastatter, L., Kuznetova, M., Singer, H., Balch, C., Weimer, D., ...
 617 Weigel, R. (2013). Community-wide validation of geospace model ground mag-
 618 netic field perturbation predictions to support model transition to operations.
 619 *Space Weather*, *11*, 369-385. doi: 10.1002/swe.20056
- 620 Raeder, J., Berchem, J., & Ashour-Abdalla, M. (1996). The importance of small
 621 scale processes in global MHD simulations: Some numerical experiments. In
 622 T. Chang & J. R. Jasperse (Eds.), *The physics of space plasmas* (Vol. 14,
 623 p. 403). Cambridge, Mass..
- 624 Raeder, J., Walker, R. J., & Ashour-Abdalla, M. (1995). The structure of the dis-
 625 tant geomagnetic tail during long periods of northward IMF. *Geophys. Res.
 626 Lett.*, *22*, 349–352.
- 627 Ridley, A., Gombosi, T., & Dezeew, D. (2004, February). Ionospheric control of the
 628 magnetosphere: conductance. *Annales Geophysicae*, *22*, 567-584. doi: 10.5194/
 629 angeo-22-567-2004
- 630 Schindler, K. (1974). A theory of the substorm mechanism. *Journal of Geophysical
 631 Research*, *79*(19), 2803–2810.
- 632 Shou, Y., Tenishev, V., Chen, Y., Toth, G., & Ganushkina, N. (2021). Magneto-
 633 hydrodynamic with adaptively embedded particle-in-cell model: Mhd-aepic.
 634 *Journal of Computational Physics*, 110656.
- 635 Slavin, J., Baker, D., Craven, J., Elphic, R., Fairfield, D., Frank, L., ... others (1989).
 636 Cdaw 8 observations of plasmoid signatures in the geomagnetic tail: An assess-
 637 ment. *Journal of Geophysical Research: Space Physics*, *94*(A11), 15153–15175.
- 638 Slavin, J., Lepping, R., Gjerloev, J., Fairfield, D., Hesse, M., Owen, C., ... Mukai,
 639 T. (2003). Geotail observations of magnetic flux ropes in the plasma sheet.
 640 *Journal of Geophysical Research: Space Physics*, *108*(A1), SMP–10.
- 641 Sokolov, I. V., Timofeev, E. V., Sakai, J. I., & Takayama, K. (1999). On shock cap-
 642 turing schemes using artificial wind. *Shock Waves*, *9*, 423–426.
- 643 Toffoletto, F., Sazykin, S., Spiro, R., & Wolf, R. (2003). Inner magnetospheric mod-
 644 eling with the Rice Convection Model. *Space Sci. Rev.*, *107*, 175-196. doi: 10
 645 .1023/A:1025532008047
- 646 Torbert, R., Burch, J., Phan, T., Hesse, M., Argall, M., Shuster, J., ... others (2018).
 647 Electron-scale dynamics of symmetric magnetic reconnection diffusion region
 648 in space. *Science*, *362*(6421), 1391–1395.
- 649 Tóth, G., Jia, X., Markidis, S., Peng, B., Chen, Y., Daldorff, L., ... Dorelli, J.
 650 (2016). Extended magnetohydrodynamics with embedded particle-in-cell
 651 simulation of ganymede’s magnetosphere. *J. Geophys. Res.*, *121*. doi:
 652 10.1002/2015JA021997
- 653 Tóth, G., Ma, Y. J., & Gombosi, T. I. (2008). Hall magnetohydrodynamics on block
 654 adaptive grids. *J. Comput. Phys.*, *227*, 6967-6984. doi: 10.1016/j.jcp.2008.04

655 .010

- 656 Tóth, G., van der Holst, B., Sokolov, I. V., Zeeuw, D. L. D., Gombosi, T. I., Fang,
657 F., ... Opher, M. (2012). Adaptive numerical algorithms in space weather
658 modeling. *J. Comput. Phys.*, *231*, 870–903. doi: 10.1016/j.jcp.2011.02.006
- 659 Tóth, G., Zeeuw, D. L. D., Gombosi, T. I., Manchester, W. B., Ridley, A. J.,
660 Sokolov, I. V., & Roussev, I. I. (2007). Sun to thermosphere simulation of
661 the October 28-30, 2003 storm with the Space Weather Modeling Framework.
662 *Space Weather Journal*, *5*, S06003. doi: 10.1029/2006SW000272
- 663 Tsutomu, T., & Teruki, M. (1976). Flapping motions of the tail plasma sheet in-
664 duced by the interplanetary magnetic field variations. *Planetary and Space*
665 *Science*, *24*(2), 147–159.
- 666 Volwerk, M., Andre, N., Arridge, C., Jackman, C., Jia, X., Milan, S. E., ... others
667 (2013). Comparative magnetotail flapping: An overview of selected events at
668 earth, jupiter and saturn. In *Annales geophysicae* (Vol. 31, pp. 817–833).
- 669 Webster, J., Burch, J., Reiff, P., Daou, A., Genestreti, K., Graham, D. B., ... others
670 (2018). Magnetospheric multiscale dayside reconnection electron diffusion
671 region events. *Journal of Geophysical Research: Space Physics*, *123*(6), 4858–
672 4878.
- 673 Wolf, R. A., Harel, M., Spiro, R. W., Voigt, G., Reiff, P. H., & Chen, C. K.
674 (1982). Computer simulation of inner magnetospheric dynamics for the
675 magnetic storm of July 29, 1977. *J. Geophys. Res.*, *87*, 5949-5962. doi:
676 10.1029/JA087iA08p05949
- 677 Wu, C. C., Walker, R., & Dawson, J. M. (1981). A three-dimensional MHD model of
678 the Earth’s magnetosphere. *Geophys. Res. Lett.*, *8*, 523–526.
- 679 Zhou, H., Tóth, G., Jia, X., & Chen, Y. (2020). Reconnection-driven dynam-
680 ics at ganymede’s upstream magnetosphere: 3-d global hall mhd and mhd-
681 epic simulations. *Journal of Geophysical Research: Space Physics*, *125*(8),
682 e2020JA028162.
- 683 Zhou, H., Tóth, G., Jia, X., Chen, Y., & Markidis, S. (2019). Embedded kinetic sim-
684 ulation of ganymede’s magnetosphere: Improvements and inferences. *Journal*
685 *of Geophysical Research: Space Physics*, *124*(7), 5441–5460.

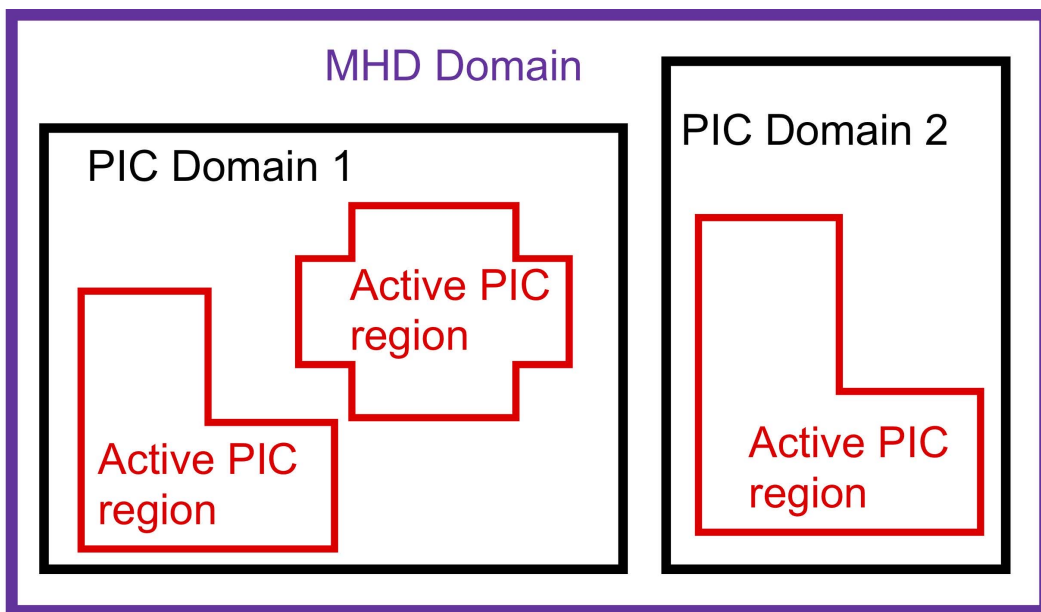


Figure 1. The schematic plot of the FLEKS adaptive grid. The red line boundary shows the flexibility of turning on and off the PIC patches during the simulation.

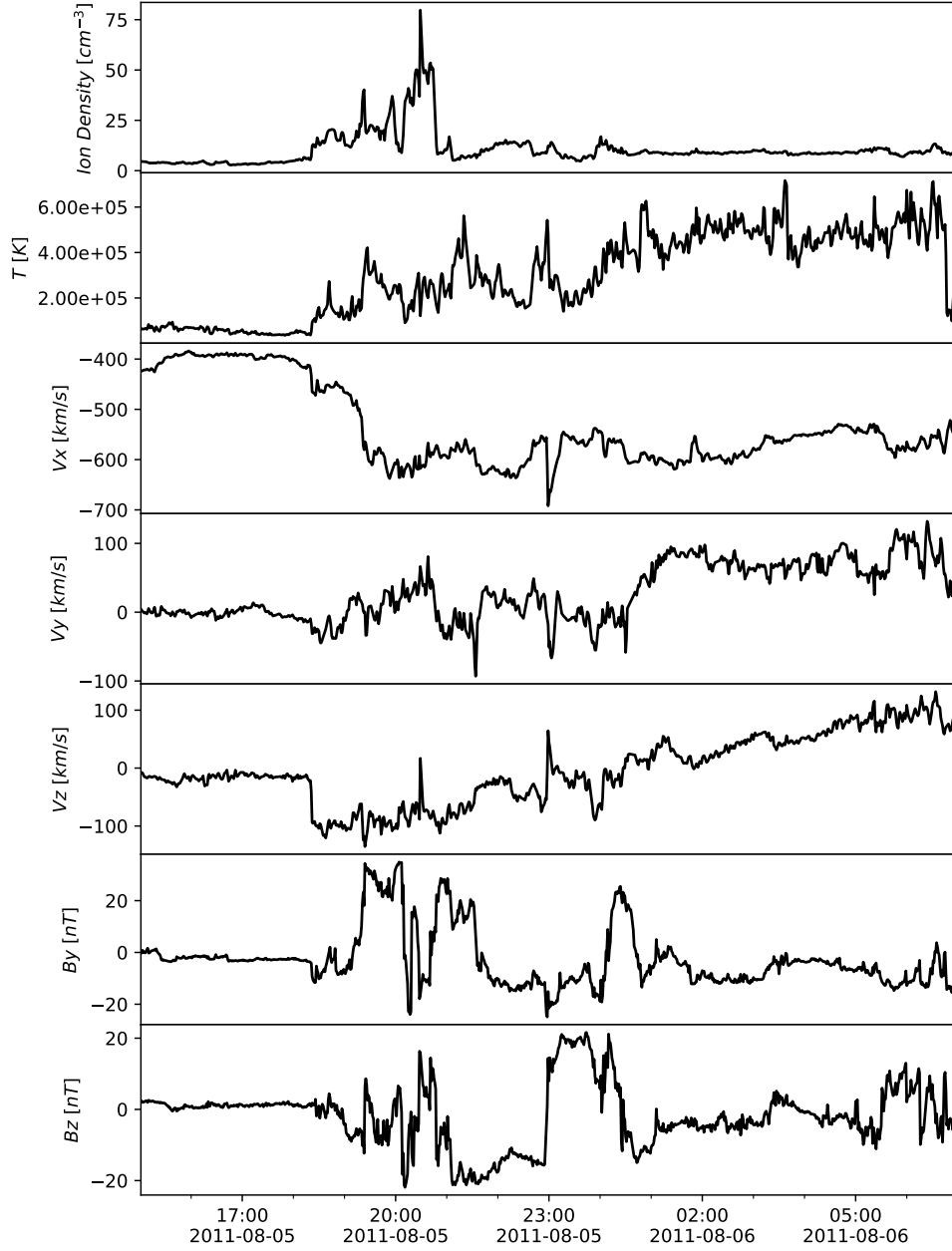


Figure 2. The solar wind bulk plasma and interplanetary magnetic field input in Geocentric Solar Magnetospheric coordinates (from top panel to the bottom: plasma density, plasma temperature, x , y and z components of the plasma flow velocity, y and z components of the magnetic field) for the simulation in this paper. The x -component of the magnetic field is set to be 0. The solar wind data is obtained from the ACE spacecraft observation and propagated to the bow shock position (Pulkkinen et al., 2013).

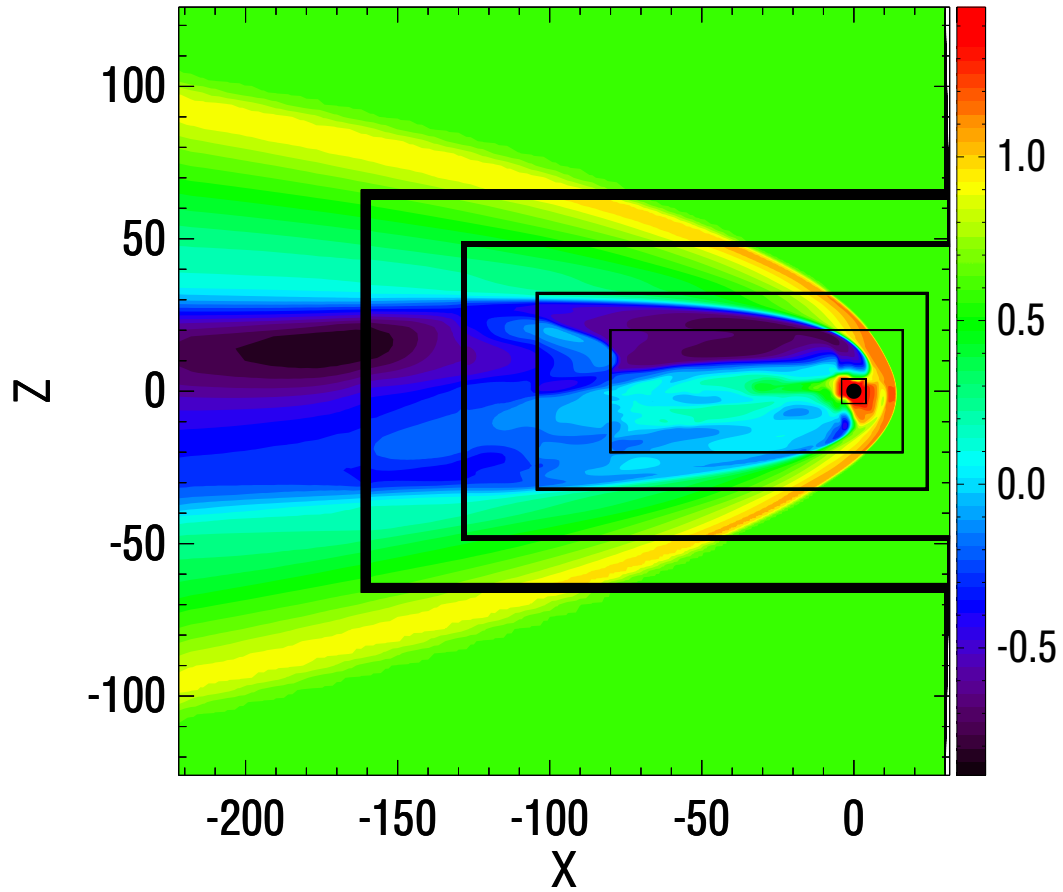


Figure 3. The meridional plane of the simulation domain. The color contour shows the plasma density of the steady state on a logarithmic scale. The black lines show the boundaries between different refinement levels. The refinement ratio between two adjacent levels is 2. The grid resolution near Earth is $1/8 R_E$ it is $1/4 R_E$ on the dayside and the magnetotail out to $x > -80 R_E$.

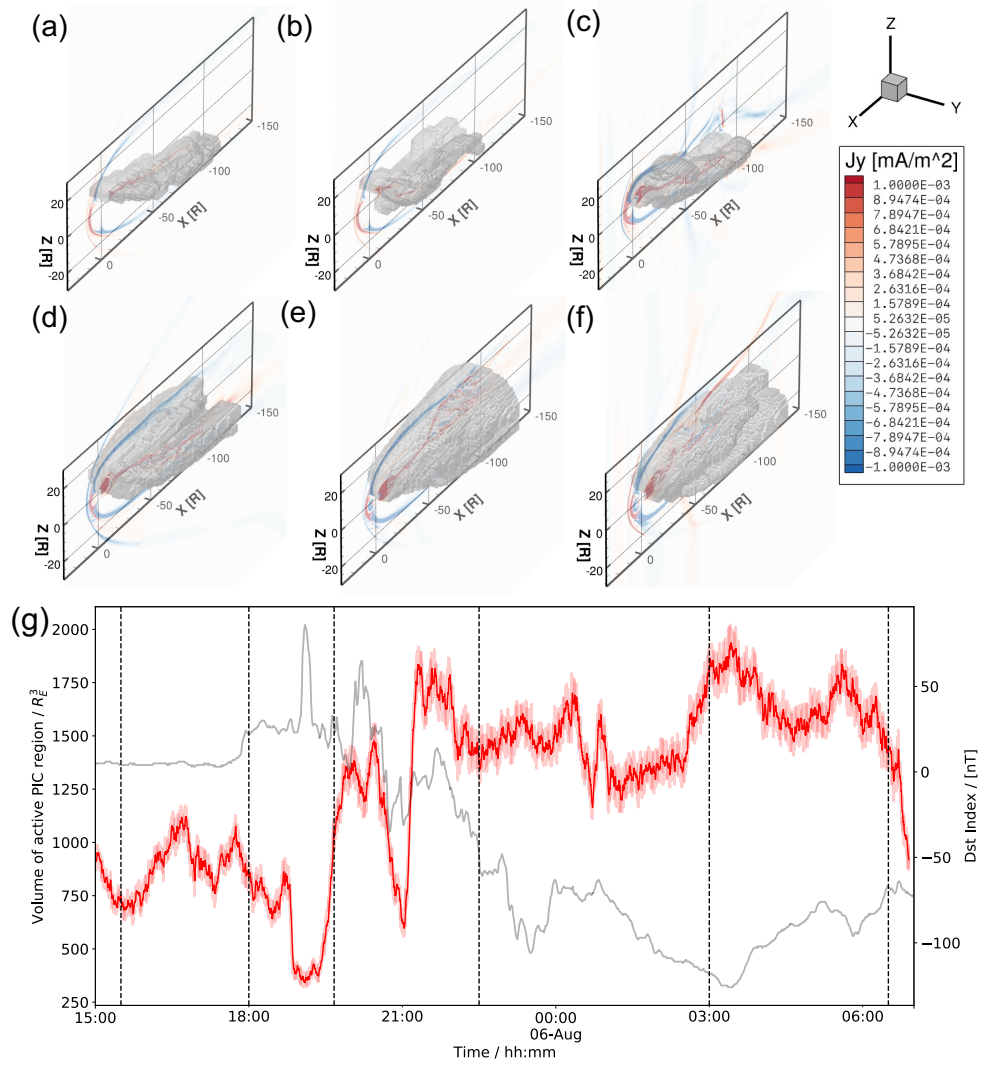


Figure 4. (a-f) Demonstration of PIC region adaptation during the simulation. The contour plot of j_y in the meridional plane is showing the general condition of the magnetospheric current system. The active PIC region boundary is shown by a gray isosurface. (g) Time evolution of the active PIC region volume (red line). The Dst index is plotted as a gray line for reference. The six vertical dashed lines correspond to the times of the snapshots (a)-(f), respectively.

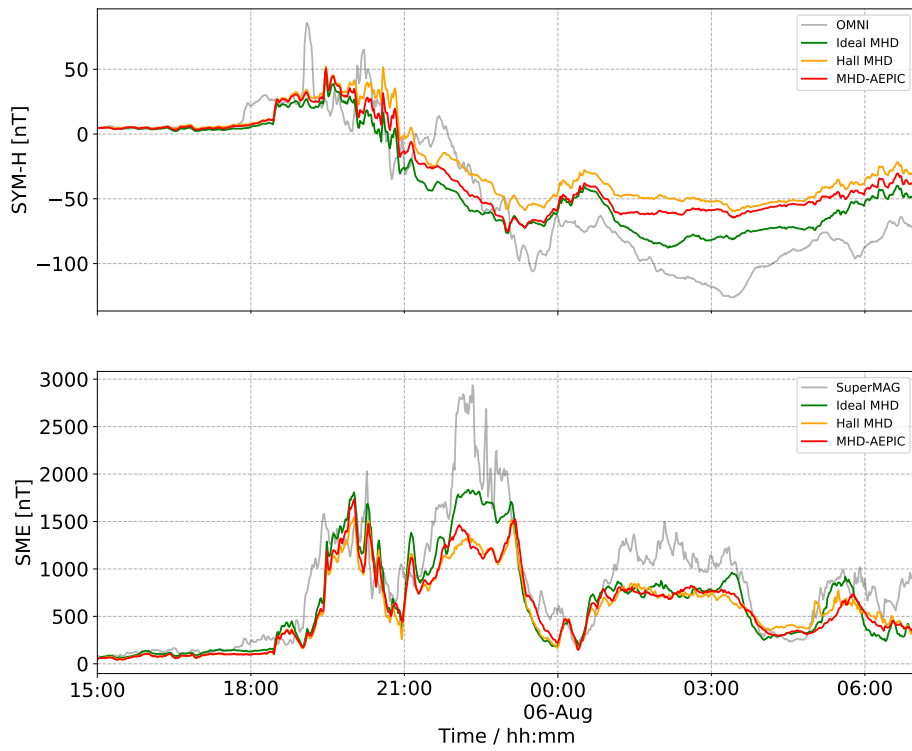


Figure 5. Aug. 6 2011 storm. Colored lines show the SYM-H and SuperMAG electrojet (SME) indexes from three different models and the gray line corresponds to the observed indexes.

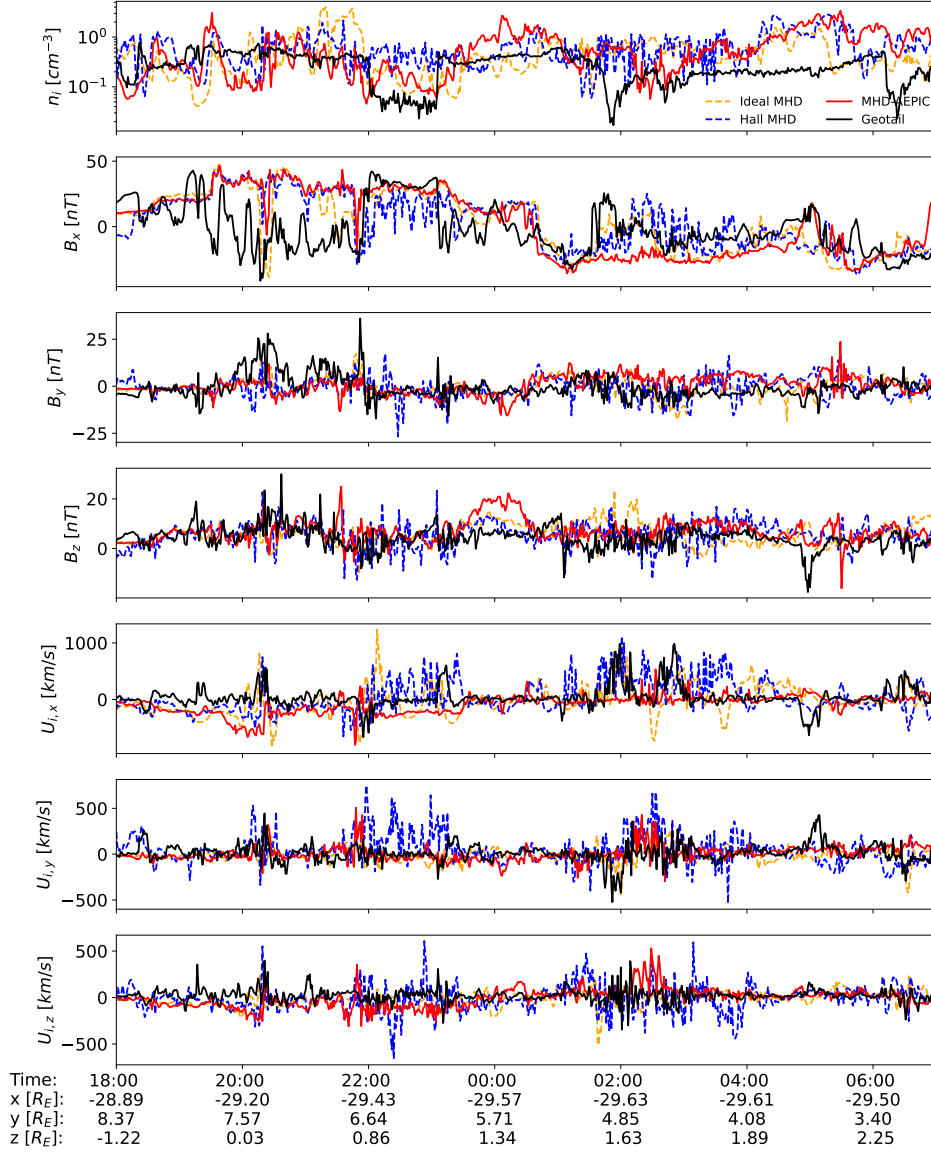


Figure 6. The ion density, magnetic field components and the ion velocity components observed by the Geotail spacecraft and the SWMF ideal MHD, Hall MHD and MHD-AEPIC simulations. The time interval shown starts from $t = 2011-08-05$ 18:00:00 right before the sudden commencement to $t = 2011-08-06$ 00:07:00 at the beginning of the recovery phase of the geomagnetic storm. The bottom X axis shows the GSE coordinates of the spacecraft at various times.

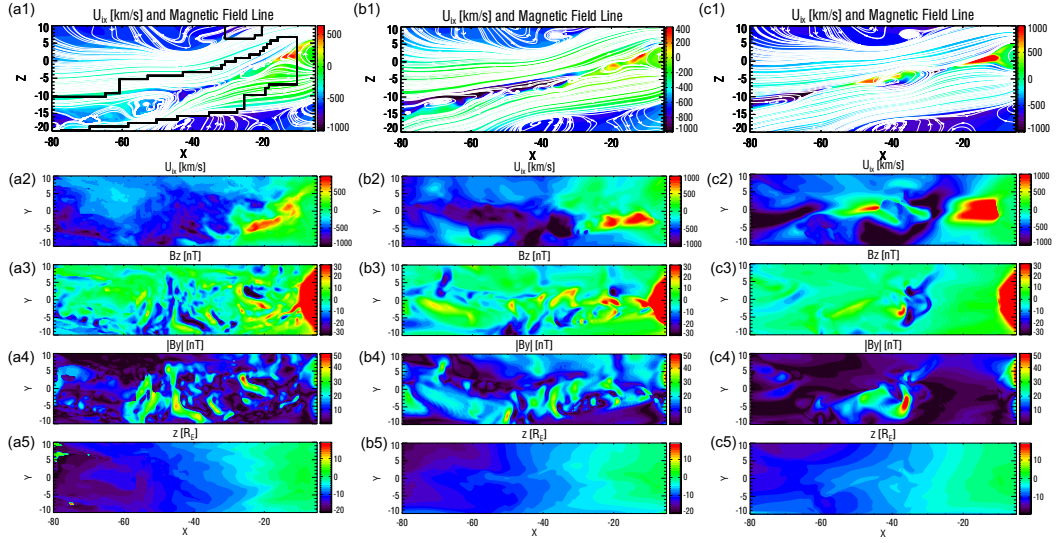


Figure 7. (a1) The x component of the ion bulk velocity $u_{i,x}$ and magnetic field lines on the meridional plane from the MHD-AEPIC simulation. The black line shows the boundary of the active PIC region. (a2) $u_{i,x}$ on the current sheet surface projected on the x - y plane. (a3) The contour plot of the B_z on the current sheet surface, color saturated at ± 30 nT. (a4) The absolute value of B_y on the current sheet surface. A pair of positive and negative B_z along with a core B_y indicates a flux rope structure. (a5) The z coordinate of the current sheet surface in the unit of R_E . (b1)-(b5) are same quantities from the Hall MHD and (c1)-(c5) are from the ideal MHD simulation. All snapshots are taken at the same time 2011-08-05 19:40:00.

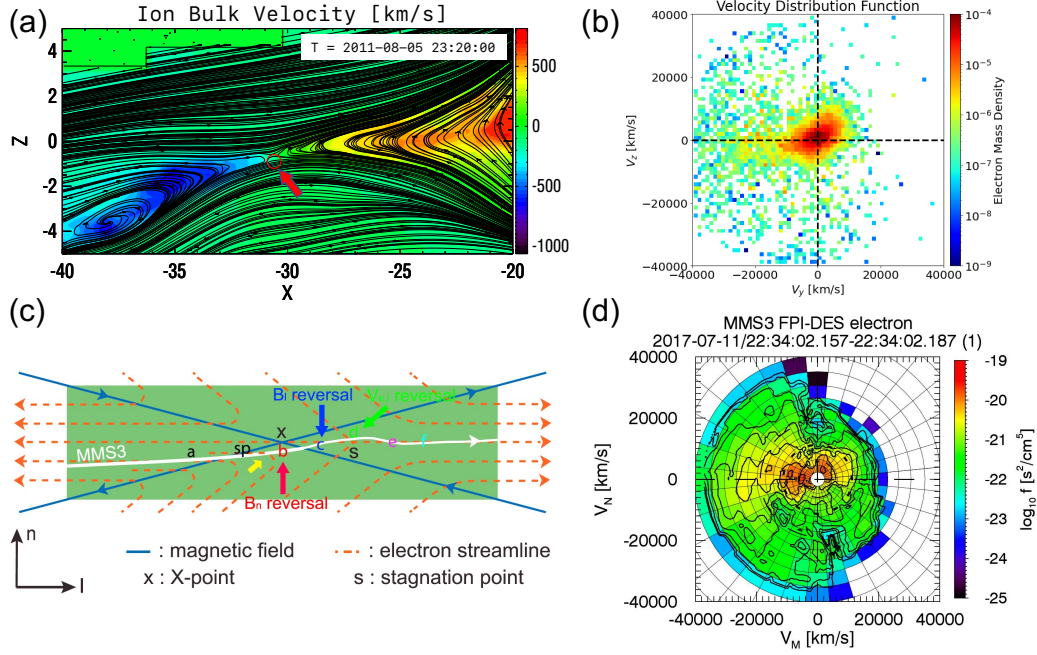


Figure 8. (a) The contour plot of the ion bulk velocity overplotted with magnetic field lines. The 2D cut is taken on the meridional plane. The red rectangle is the position where the electrons for the VDF are collected. Notice that some area at upper left is not covered by PIC which illustrates the AEPIC feature. (b) The electron VDF from the simulation, colored in electron mass density in log scale. (c) A sketch (Figure 1 (b) in Hwang et al. (2019)) demonstrating possible magnetic field geometries. The white curve represents a possible MMS3 trajectory. The electron VDF in (d) is taken at the position b pointed by a red arrow. (d) MMS3 observation (Figure 2 (c) in Hwang et al. (2019)).